Supporting Information for

Rapid Vapor-Phase Deposition of High-Mobility *p*-Type Buffer Layers on Perovskite Photovoltaics for Efficient Semi-Transparent Devices

Robert A. Jagt[†], Tahmida N. Huq[†], Sam A. Hill[†], Maung Thway[‖], Tianyuan Liu[‖], Mari Napari[†,‡],

Bart Roose[§], Krzysztof Gałkowski[§], Weiwei Li[¹], Serena Fen Lin[‖], Samuel D. Stranks[§,¥], Judith L.

MacManus-Driscoll[†], Robert L. Z. Hoye[‖,†,]*

[†] Department of Materials Science and Metallurgy, University of Cambridge, 27 Charles

Babbage Road, Cambridge CB3 0FS, UK

[‡] Present address: Zepler Institute for Photonics and Nanoelectronics, University of

Southampton, University Road, Southampton SO17 1BJ, UK

[‖] Solar Energy Research Institute of Singapore, National University of Singapore, Singapore

117574

[§] Department of Physics, Cavendish Laboratory, University of Cambridge, 19 JJ Thomson

Avenue, Cambridge CB3 0HE, UK

[¥] Department of Chemical Engineering and Biotechnology, University of Cambridge, Philippa

Fawcett Drive, Cambridge CB3 0AS, UK

[!!] *Present address: Department of Materials, Imperial College London, Exhibition Road, London SW7 2AZ, UK*

AUTHOR INFORMATION

[*]**Corresponding Author**

Email: r.hoye@imperial.ac.uk

S1. Experimental

Growth of CuO_x by AP-CVD: The oxide films were grown using the Vertical Cambridge University Close Proximity (V-CUCP) reactor described in our previous work.[1] The metal precursor used was Allyloxytrimethylsilyl Hexafluoroacetylacetonate Copper(I), which is also known by its commercial name, Cupraselect®. Similar to other CVD/ALD precursors, care needs to be taken in handling Cupraselect®. For safety reasons, the precursor is filled into the sealed glass bubbler inside a nitrogen-filled glovebox, and depositions are performed inside a well-ventilated fume hood. However, it should be noted that the CVD precursor is not pyrophoric and does not give noxious or acutely hazardous gaseous by-products, making it relatively mild compared to other CVD/ALD precursors (e.g., diethylzinc or trimethylaluminium). Cupraselect® inside its glass sealed bubbler was heated to 40 °C. We introduced the metal precursor vapor to the gas manifold by bubbling 33 mL min^{-1} Ar gas (Air Products, <0.01 ppm O2, <0.02 ppm H_2O) through the liquid precursor and further diluting it with 66 mL min^{-1} Ar gas. For the oxidant water vapor was used and was produced by bubbling Ar gas through deionized water at room temperature at a flow rate of 100 mL min^{-1}. The H_2O vapor was diluted with Ar gas flowing at 100 mL min^{-1}. Further we introduced Ar gas flowing at 1000 mL min^{-1} to the gas manifold. This was then split

between four channels that were positioned between the metal precursor and oxidant gas channels. The gas manifold was maintained at 40 °C using circulating water. The substrate was oscillated beneath the manifold at a default speed of 50 mm s^{-1}. This speed was changed if we needed to change the exposure time per cycle to determine the growth regime. We maintained a spacing of 125 μm between the bottom of the gas manifold and top of the substrate using a micrometer for all growths. The temperature of the substrate holder was adjusted to the desired value. A schematic of the V-CUCP setup can be found in Ref 1. The films were grown inside a fume hood in air. The samples were stored inside dry cabinet (<1% relative humidity) before further characterization or ITO sputtering. The measurements or ITO deposition were typically performed within a day of depositing the CuO_x films.

Fabrication of perovskite thin films: The triple-cation perovskite films were deposited from a precursor solution containing 1 mol L^{-1} $CH(NH_2)_2I$ (GreatCell Solar, 90-100%w/w), 0.2 mol L^{-1} CH_3NH_3Br (GreatCell Solar, 90-100%w/w), 1.1 mol L^{-1} PbI_2 (TCI, 99.99%) and 0.2 mol L^{-1} $PbBr_2$ (TCI, ≥98.0%) were dissolved in 51 vol.% N,N-dimethylformamide (Sigma-Aldrich, 99.8%), 34 vol.% dimethyl sulfoxide (Sigma-Aldrich, ≥99.9%), 15 vol.% 1-methyl-2-pyrrolidone (Sigma-Aldrich, 99.5%). We also prepared at 1.5 mol L^{-1} stock solution of CsI (Sigma-Aldrich, 99.999%) in dimethyl sulfoxide. We added 48 μL of the CsI stock solution to the perovskite solution and mixed without heating. The films were grown on 12 mm X 12 mm substrates by spreading 40 μL solution over the substrate and spinning at 1000 rpm for 10 s, followed by 6000 rpm for 35 s. 75 μL chlorobenzene (Sigma-Aldrich, ≥99%) was dynamically dripped over the substrate 10 s before the end. The films were annealed at 100 °C for 60 min. All processing was performed inside a N_2-filled glovebox.

Electron and hole transporting layers: Solaronix FTO of 10 $\Omega \square^{-1}$ was chemically etched using 2M HCl and zinc powder for 2 minutes and subsequently cleaned with 2% Hellmanex water solution, acetone and isopropanol for 15 min each. The substrates were placed on a hotplate and heated to 450 °C. A 30 nm compact TiO_2 layer was deposited using spray pyrolysis. For the precursor 0.4 mL acetylacetone and 0.6 mL titanium diisopropoxide bis(acetylacetonate) are diluted in 9 mL anhydrous ethanol. After the spray pyrolysis the hotplate was left to cool down naturally to room temperature. Subsequently a mesoporous TiO_2 layer was grown by spreading 40 μL solution (150 mg TiO_2 paste (Dyesol 30 NR-D) dissolved in 1 mL anhydrous ethanol) over the substrate and spinning at 4000 rpm for 10 s (2000 rpm ramp). After spin coating the substrates were placed on heat up to 450 °C with a 40 min ramp time and annealed for 30 minutes and let cooled down naturally. The TiO_2 was subsequently treated with Li-TFSI as described in the supplementary of Ref 2. The hole transport layer was deposited by spin coating a solution containing PTAA (10 mg PTAA in 964 μL toluene) doped with 16 μL mL^{-1} 0.18M Li-TFSI in acetonitrile, as well as 20 μl mL^{-1} of 10% TBP (*i.e.*, solution of 100 μL TBP + 900 μL toluene) at 4000 rpm for 20 s.

DC magnetron sputtering of ITO: The ITO transparent contacts were deposited in a high-vacuum sputtering system by DC-magnetron sputtering using a target of In_2O_3 (90 wt%) / SnO_2 (10 wt%) (99.99% pure, Testbourne Ltd). During sputtering, the chamber pressure was maintained at 2.0 Pa under a flow rate of 1.2 mL min^{-1} Ar and was conditioned by pre-sputtering for 12 min. The active area of sputtering was measured to be 13.75 cm^2 and power density was 4.4 W cm^{-2} (total power 60 W). The depositions were performed in three consecutive steps lasting 1 min 40 s each. The sheet resistance of the as-deposited films on glass was 9.2 $\Omega \square^{-1}$, as measured by a four point probe.

X-ray diffraction measurements: X-ray diffraction was performed using a Bruker D8 theta/theta system. Cu K$_\alpha$ radiation (λ = 1.5406 Å) was used as the X-ray source.

Scanning electron microscopy: All electron microscopy images were taken on a FEI Nova NanoSEM.

Atomic force microscopy: The film thickness was measured using a Dektak profilometer. A step-edge in the oxide film was created through selective-area deposition, by drawing over a portion of the substrate using marker fluid and removing the marker after the growth of the oxide using acetone. Atomic force microscopy measurements were performed using a Bruker Multimode 8. Silicon tips were used with a cantilever resonant frequency of 319 kHz

X-ray photoemission spectroscopy: X-ray photoemission spectroscopy was undertaken by a monochromatic Al Kα x-ray source (hν=1486.6 eV) using a SPECS PHOIBOS 150 electron energy analyzer with a total energy resolution of 0.5 eV. The measurements were performed at 300 K.

Ultraviolet-visible spectroscopy: The total transmittance (*T*) and reflectance (*R*) spectra were acquired using a ultraviolet-visible-near infrared spectrophotometer (Shimadzu UV-3600) equipped with an integrating sphere.

Kelvin probe microscopy: The work function was measured using a Relative Humidity Kelvin Probe System (RHC040, KP Technology Ltd.), which measured the contact potential difference between the sample surface and a cylindrical stainless steel alloy tip (2 mm diameter). The samples were prepared under dry N_2 conditions and transferred to the glovebox containing the Kelvin Probe. The glovebox had continuous N_2 flow. Measurements of the contact potential difference were made in the dark and after the relative humidity inside the glovebox stabilized to below 1%. The contact potential difference measurements were made for at least 80 min until the measurements stabilized in value. Three measurements were made for each sample and the results averaged.

Time resolved photoluminescence measurements: Time-resolved photoluminescence measurements were performed by exciting the samples using a 400 nm wavelength frequency-doubled Ti:Sapphire laser (Spectra Physics Solstice). The repetition rate was 1 kHz and pulse length approximately 100 fs. The photoluminescence spectra were measured at 5 ns time intervals using an intensified charge-coupled device camera with an Andor iStar DH740 CCI-010 system connected to a grating spectrometer (Andor SR303i).

Perovskite solar cell characterization: Solar simulations were performed using an ABET Technologies Sun 2000 Solar Simulator and Keithley 2623A source-measure unit. The light source was a 450 W xenon lamp (Oriel) equipped with a Schott-K113 Tempax sunlight filter (Präzisions Glas & OptikGmbH) to match the emission spectrum of the lamp to the AM1.5G standard. The devices were all illuminated from the substrate (glass/FTO/TiO$_x$) side. Before measuring the devices, the solar simulator was calibrated with a silicon reference diode equipped with an infrared

cut-off filter (KG-3, Schott). The scan rate was 100 mV s^{-1}. The active area was 3 mm^2 for the semi-transparent devices and 4.15 mm^2 for the opaque devices. The devices were masked using an Al mask to prevent edge effects. External quantum efficiency spectra were recorded as a function of wavelength under a constant white-light bias of approximately 5 mW cm^{-2} supplied by an array of white light-emitting diodes. The excitation beam coming from a 300 W xenon lamp (ILC Technology) was focused through a Gemini-180 double monochromator (Jobin Yvon Ltd) and chopped at approximately 2 Hz. The signal was recorded using a Model SR830 DSP lock-in amplifier (Stanford Research Systems).

p-type PERC fabrication: The p-type Czochralski c-Si substrates (190 μm, 1-2 Ω cm) with the size of 244.3 cm^2 (M2) were used. The wafers were first saw damage etched (SDE) in a potassium hydroxide (KOH) solution prior to industrial standard RCA (Radio Corporation of America) cleaning. The cleaned wafers were then masked on the rear with silicon nitride (SiN$_x$) using plasma enhanced chemical vapor deposition (PECVD, MAiA, Meyer Burger). This was to protect the rear surface during the chemical texturing of the front. The masked samples were dipped in alkaline texturing solution bath. After front side texturing, the samples were again cleaned using RCA solutions and mild hydrofluoric acid (2% conc.). The emitter isolation was achieved by blocking the phosphorus diffusion using SiN$_x$ mask. A full area mask was applied on the front surface of the wafer. A nanosecond (ns) green laser (ILS LT, Innolas Solutions) was used to selectively ablate the SiN$_x$ mask to open windows for diffusion. The phosphorus was diffused into the front surface to form n+ emitter by standard POCL$_3$ diffusion (Quantum, Tempress). Following the diffusion step, the phosphosilicate glass (PSG) layer (formed during the diffusion process) and the rear SiN$_x$ mask are removed together in hot HF acid (10% concentration). The RCA cleaning steps are then

repeated before the passivation step. The same PECVD tool used for SiN_x masking is again used for passivating both front and rear surfaces of the c-Si solar cell. The front ARC is 105 nm single layer of SiN_x. The rear passivation is $AlO_x/SiO_x/SiN_x$ stack. The rear dielectric stack is then ablated using ns green laser to form periodic groove for rear contact opening. Finally, metal contacts (commercially available Ag paste for the front and Ag-Al paste for the rear) are deposited on each side by using commercial screen-printing (Eclipse, DEK). The cells are subsequently fired at high temperature (~750°C) for front and rear contact formation.

n-type monoPoly™ fabrication: 244.3 cm^2 (M2) *n*-type c-Si wafers (190 μm, 1-2 Ωcm) were used. The wafers are first saw damage etched in a potassium hydroxide (KOH) solution. The localized active areas are produced on the substrate by masking. The non-active areas (no diffusion of boron to form p-n junction) are covered with a silicon nitride (SiN_x) mask. Random pyramids sized approximately 2-3 μm are formed on both sides of c-Si wafer by alkaline texturing. The samples are then cleaned using Radio Corporation of America (RCA) cleaning, followed by a short dip in hydrofluoric (HF) acid. The samples then undergo boron (p^+) diffusion in a commercial tube furnace. Rear surface polishing, as well as, junction removal is done using single-side etching tool in one step. Another round of RCA clean and short HF dip is performed after SiN_x masking on the front side. An intrinsic poly-Si layer is deposited with a thin layer of interfacial SiO_x (in situ deposition) using low pressure chemical vapor deposition (LPCVD) tube furnace. The intrinsic poly-Si is then doped with phosphorus to form n^+ doped poly-Si in commercial tube furnace. Since the LPCVD process is a double-sided deposition process, the poly-Si is on both sides of the substrate. The rear side is then masked using SiNx to protect the n^+ doped poly-Si during the following chemical treatments. Chemical etching such as KOH, HF and RCA are done to remove

the poly-Si deposited on the front side, as well as the mask. The plasma enhanced chemical vapor deposition (PECVD) tool is then again used to passivate the cells with AlO_x/SiN_x stack at the front and SiN_x at the rear. Metal contacts (Ag-Al for the front and Ag for the rear) are deposited on each side by commercial screen-printing. All samples are fired at ~750 °C in the industrial fast-firing furnace.

Silicon bottom cell measurements: The *I-V* measurement of silicon bottom cell was performed using commercial LEDs IV tester (Wavelabs, Sinus-220). There are 21 LEDs in the illumination source simulating the AM1.5G spectrum from the wavelength range of 300 to 1100 nm. The measurement was performed under standard testing conditions. The active area of the silicon bottom cell was defined by a shadow mask of 1 cm^2. In order to measure the efficiency of the silicon bottom cell in tandem configuration, the perovskite filter (4 cm^2) was placed on top of the silicon bottom cell. Illumination through the perovskite filter was through the glass/FTO/TiO_x side to be consistent with our semi-transparent device measurements.

Ellipsometry measurements: Spectroscopic ellipsometry measurements were performed using a J.A. Woolam Co., Inc. EC-400 system using a 75 W Xe light source. Measurements were performed at 60°, 65° and 70°. The wavelength was varied from 245 nm to 900 nm with 1 nm intervals. The Cauchy equation with non-linear optimization code was used to fit the data to obtain values for the thickness, index of refraction and extinction coefficient. For these spectroscopic ellipsometry measurements, the oxides were grown in Si substrates with a 287 nm thick SiO_2 layer (as measured spectroscopic ellipsometry).

***Hall measurements*:** Hall effect measurement were carried out with MMR Technologies Hall system using van der Pauw configuration with a 0.2 T magnetic field at room temperature.

***ToF ERDA*:** Time-of-flight elastic recoil detection analysis (ToF-ERDA) with 13.6 MeV $^{79}Br^{7+}$ ion beam was used to determine the elemental composition of the Cu_2O films.
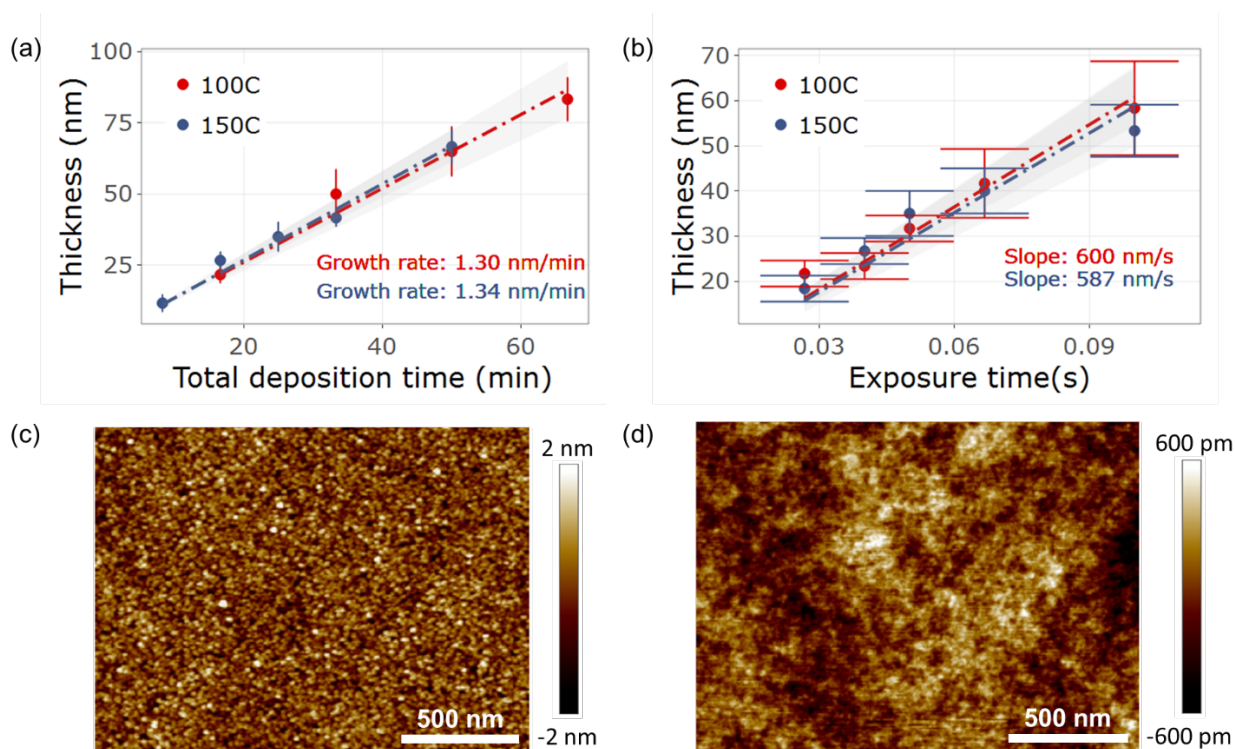
S2. Supporting Data

Figure S1. Growth properties of CuO_x on glass. The measured thickness of the CuO_x grown at 100 °C (red) and 150 °C (dark blue) as a function of (a) the total deposition time and (b) the exposure time per AP-CVD cycle. (c) AFM image of CuO_x deposited with 100 AP-CVD cycles (3 nm thickness based on the growth rate) on glass with a root mean square roughness of 0.64 nm. (d) AFM image of glass without CuO_x (root mean square roughness of 0.21 nm).
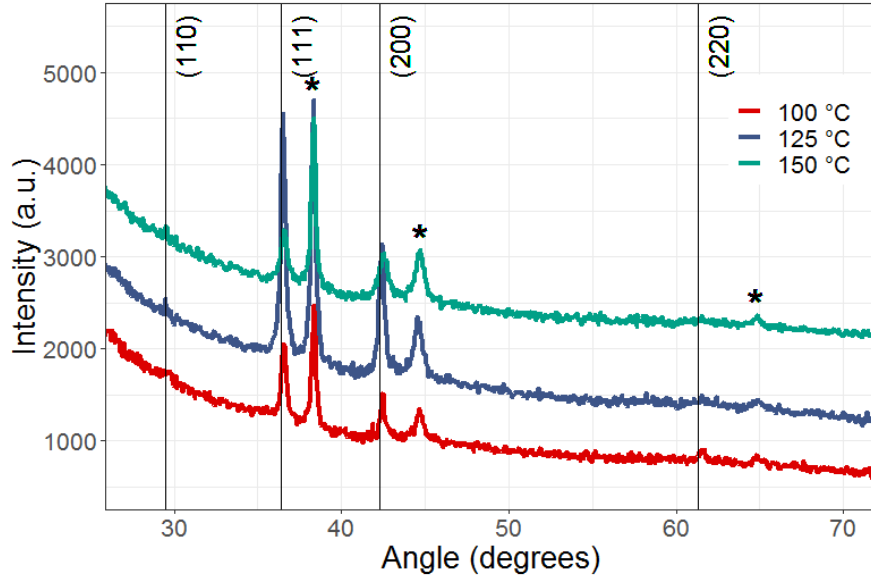
Figure S2. The X-ray diffraction data of the CuO$_x$ films grown onto glass at 100 °C (red), 125 °C (dark blue) and 150 °C (green). The vertical lines indicate the Miller indices of the Cu$_2$O phase. The * indicate peaks due to the gold contacts.
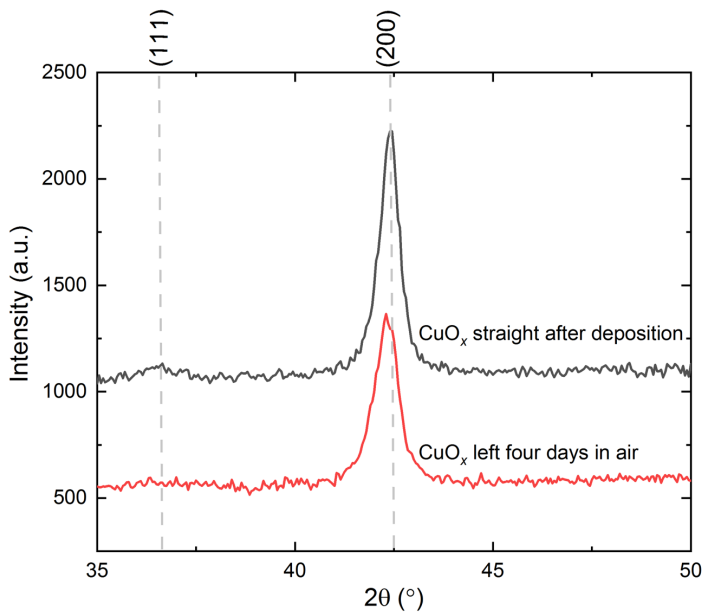
Figure S3. The X-ray diffraction patterns of the CuO$_x$ films grown onto silicon with 100 nm thermal oxide. Note that on silicon CuO$_x$ grows with preferred orientation. The vertical lines

indicate the Miller indices of the Cu_2O phase. No peaks due to CuO phase impurities were observed.
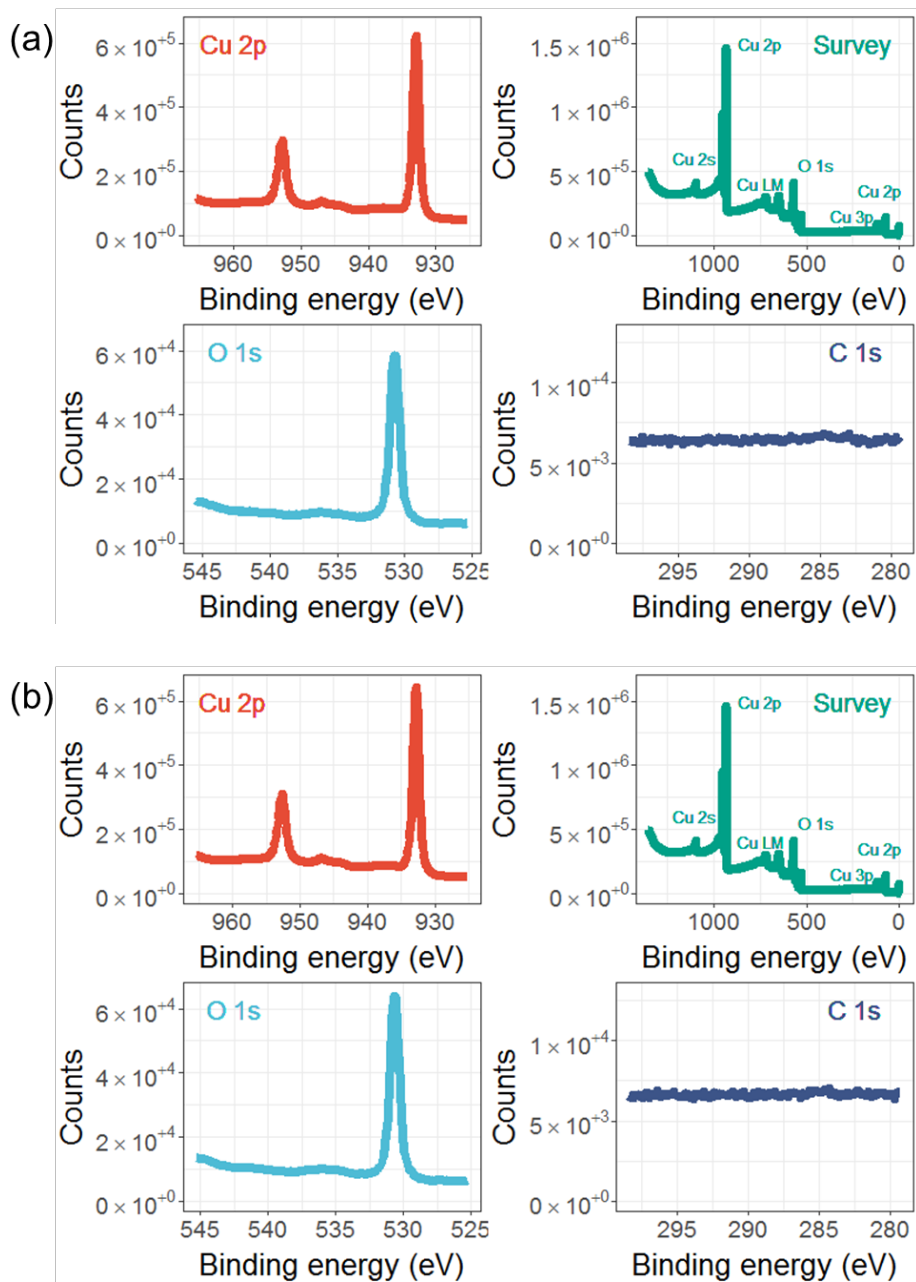
Figure S4. The X-ray photoemission spectra of the CuO_x grown at (a) 100 °C and (b) 150 °C. The colors indicate the spectral regions corresponding to the Cu 2*p* (red), O 1*s* (blue), C 1*s* (dark blue) and the survey spectrum (green).
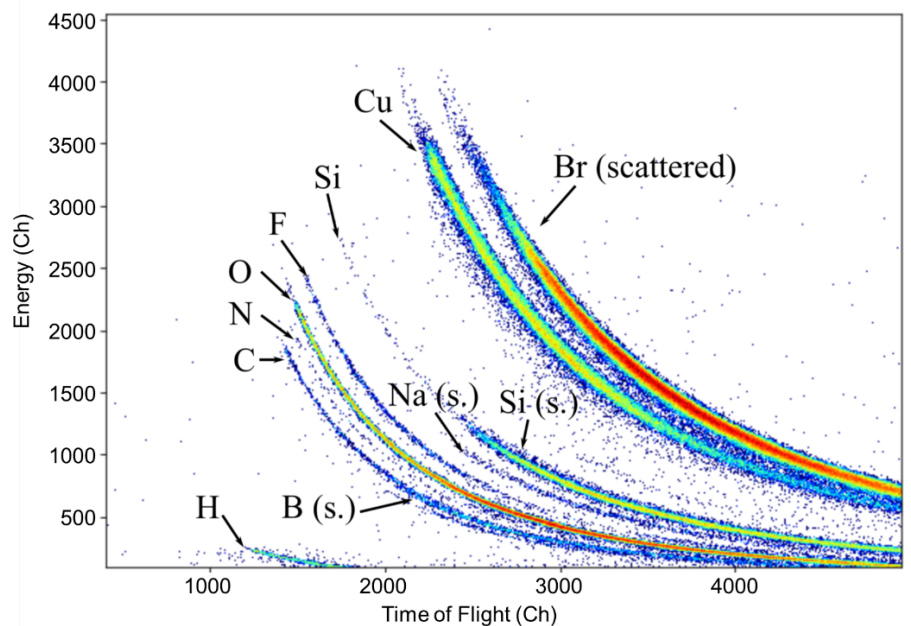
Figure S5. Energy – time of flight histogram of CuO_x sample deposited at 125 °C with H_2O vapor as the oxidant. The label '(s.)' denotes an element from the substrate instead of from the film.

Table S1. Time of Flight Elastic Recoil Detection Analysis (ToF-ERDA) measurements of the bulk composition of AP-CVD CuO_x grown at different temperatures

Deposition temperature (℃)	Cu (at.%)	O (at.%)	H (at.%)	C (at.%)	N (at.%)	F (at.%)	Si (at.%)
100	57.1±0.7	35.9±0.8	2.4±0.2	1.9±0.2	0.5±0.1	1.9±0.2	0.3±0.1
125	56.2±0.5	37.1±0.6	2.2±0.2	1.7±0.2	0.4±0.1	2.1±0.2	0.4±0.1
150	60.3±0.7	37.3±0.7	1.0±0.1	0.7±0.1	0.2±0.1	0.3±0.1	0.2±0.1
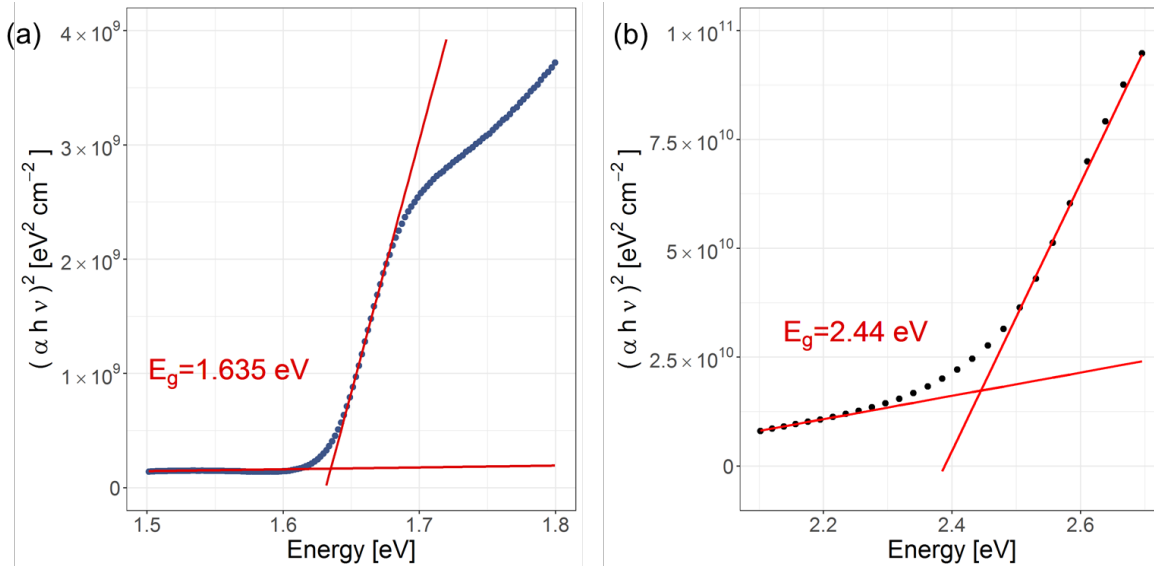
Figure S6. Tauc plot for (a) triple-cation perovskite ($Cs_{0.05}(MA_{0.17}FA_{0.83})_{0.95}Pb(I_{0.83}Br_{0.17})_3$) and (b) CuO_x thin films, obtained from UV-visible spectrophotometry measurements. The optical band gap determined is depicted in red.
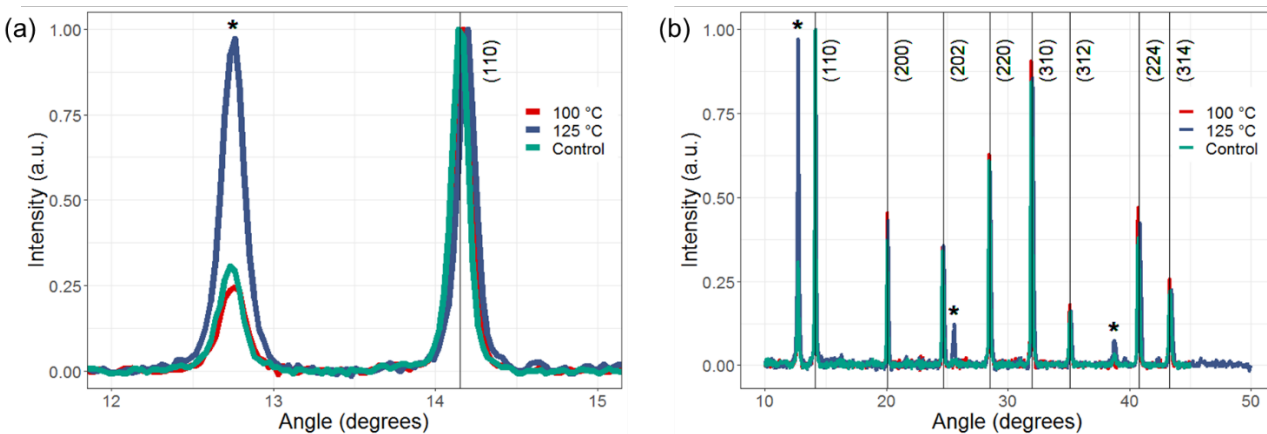

Figure S7. The measured X-ray diffraction pattern of glass/perovskite/PTAA without CuO_x (control; depicted in green) and with CuO_x deposited at 100 °C (red) and 125 °C (dark blue). (a) Close-up of the diffraction pattern at 2θ values from 12° to 15°. (b) Diffraction pattern over 2θ values from 10° to 50°. * indicates peaks from PbI_2.
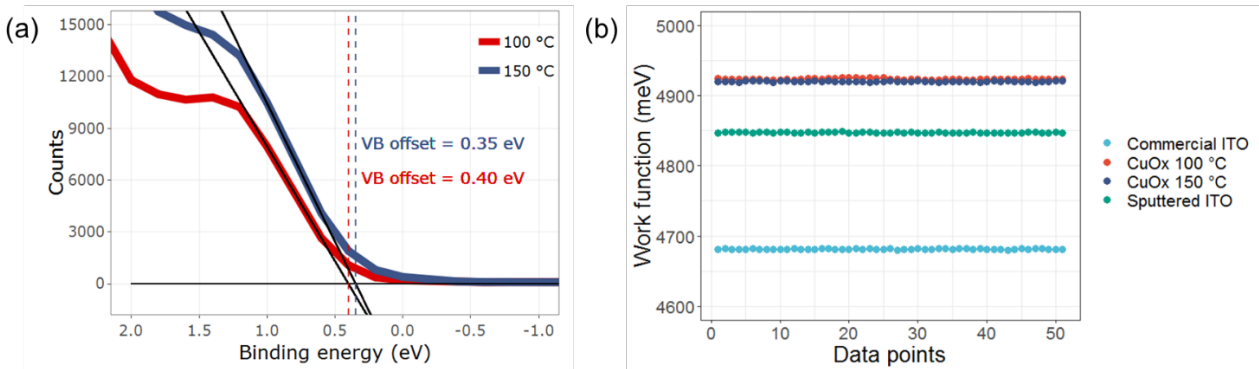
Figure S8. (a) The XPS valence band (VB) spectrum for CuO$_x$ grown at 100 °C (red) and 150 °C (blue) onto 100 nm Au onto Si. The VB offset is determined by fitting a tangent line and determining the horizontal axis intersect. (b) Measured work function for commercial ITO, CuO$_x$ grown at 100 °C onto 100 nm Au onto Si, CuO$_x$ grown at 150 °C onto 100 nm Au onto Si and sputtered ITO.
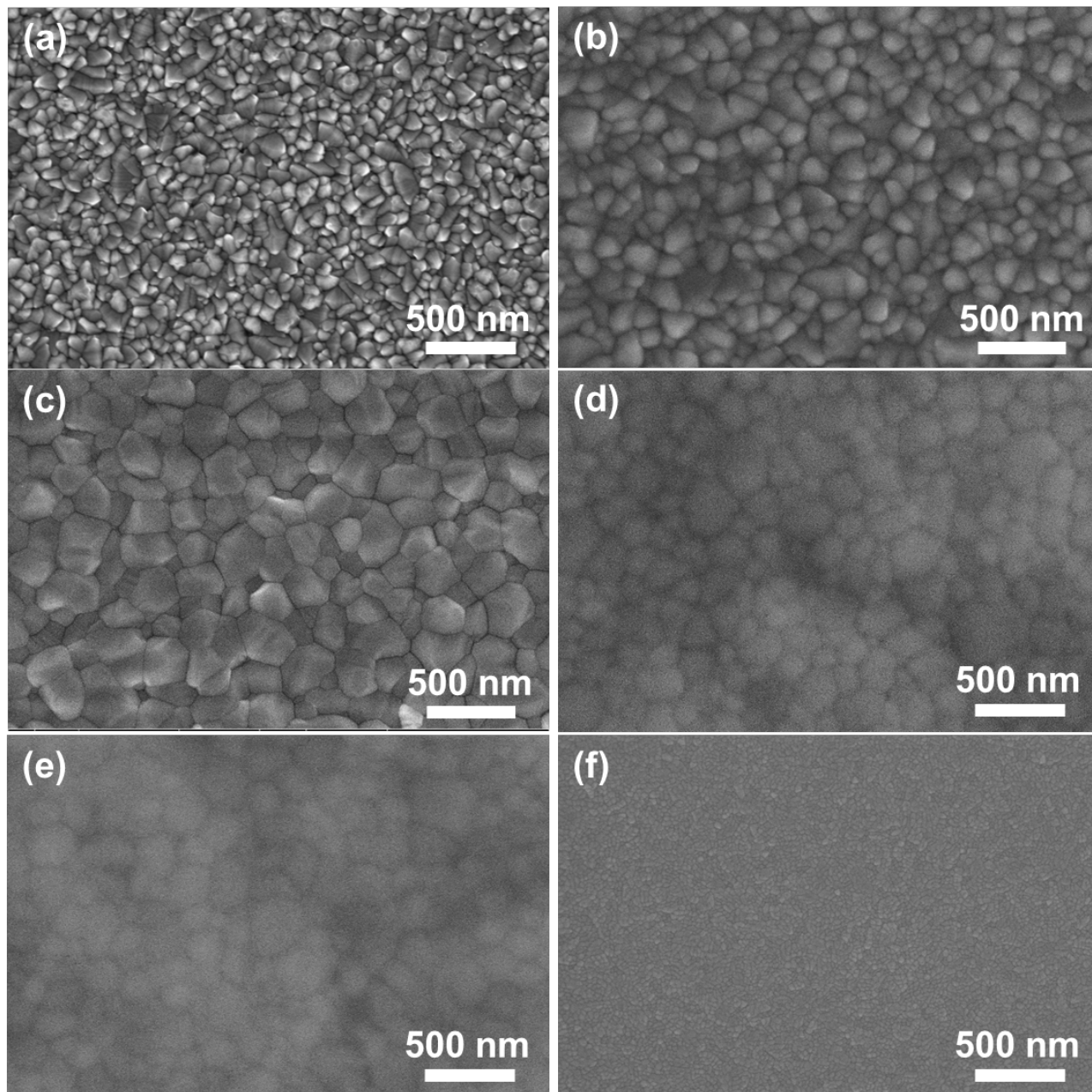
Figure S9. Top down sequential SEM figures of the device stack: (a) FTO substrate, (b) TiO_x compact layer, (c) triple-cation perovskite absorber layer, (d) PTAA hole transport layer, (e) CuO_x layer, and (f) finally with the ITO layer.
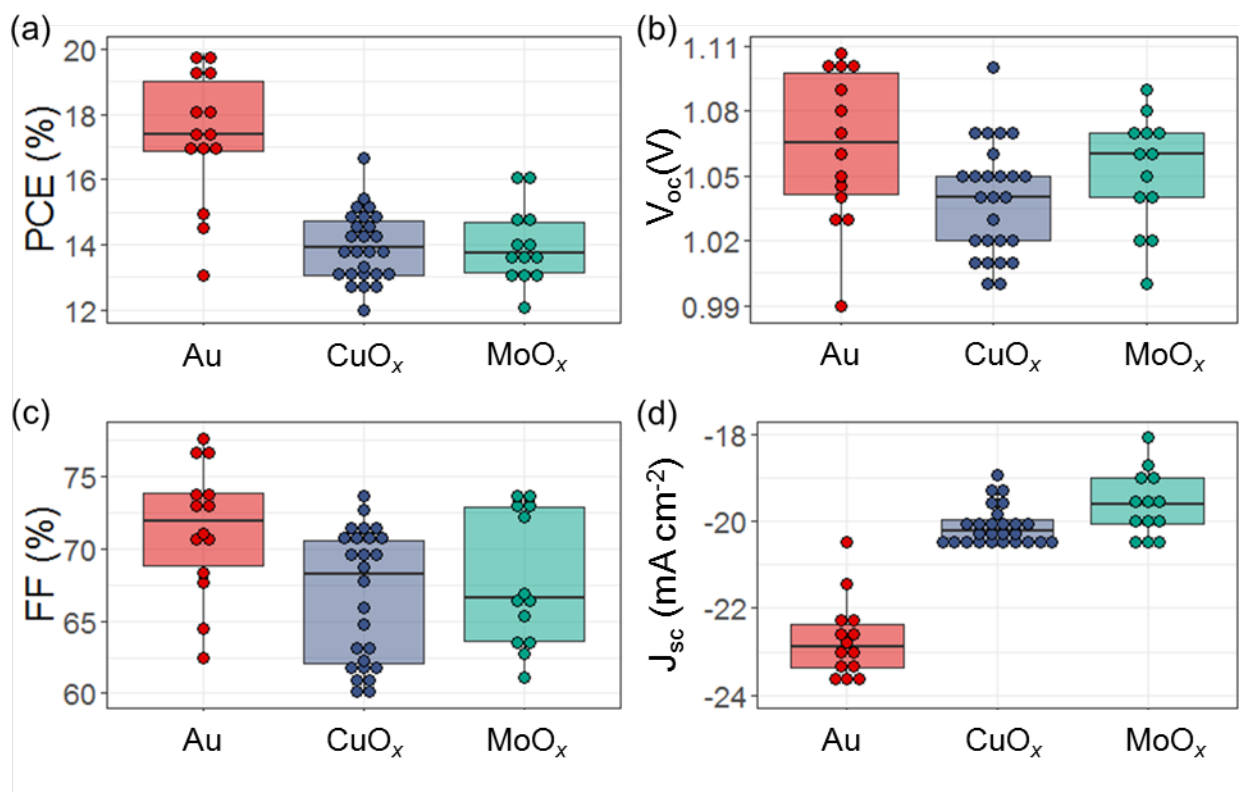
Figure S10. Boxplots summarizing the photovoltaic (PV) performance of the opaque (red; 14 devices), semi-transparent devices with CuO_x buffer layer (dark blue; 24 devices) and with a MoO_x buffer layer (green; 15 devices). The PV properties are the (a) power conversion efficiency, (b) open circuit voltage (V_{OC}), (c) fill factor (FF) and (d) short circuit current density (J_{SC}).
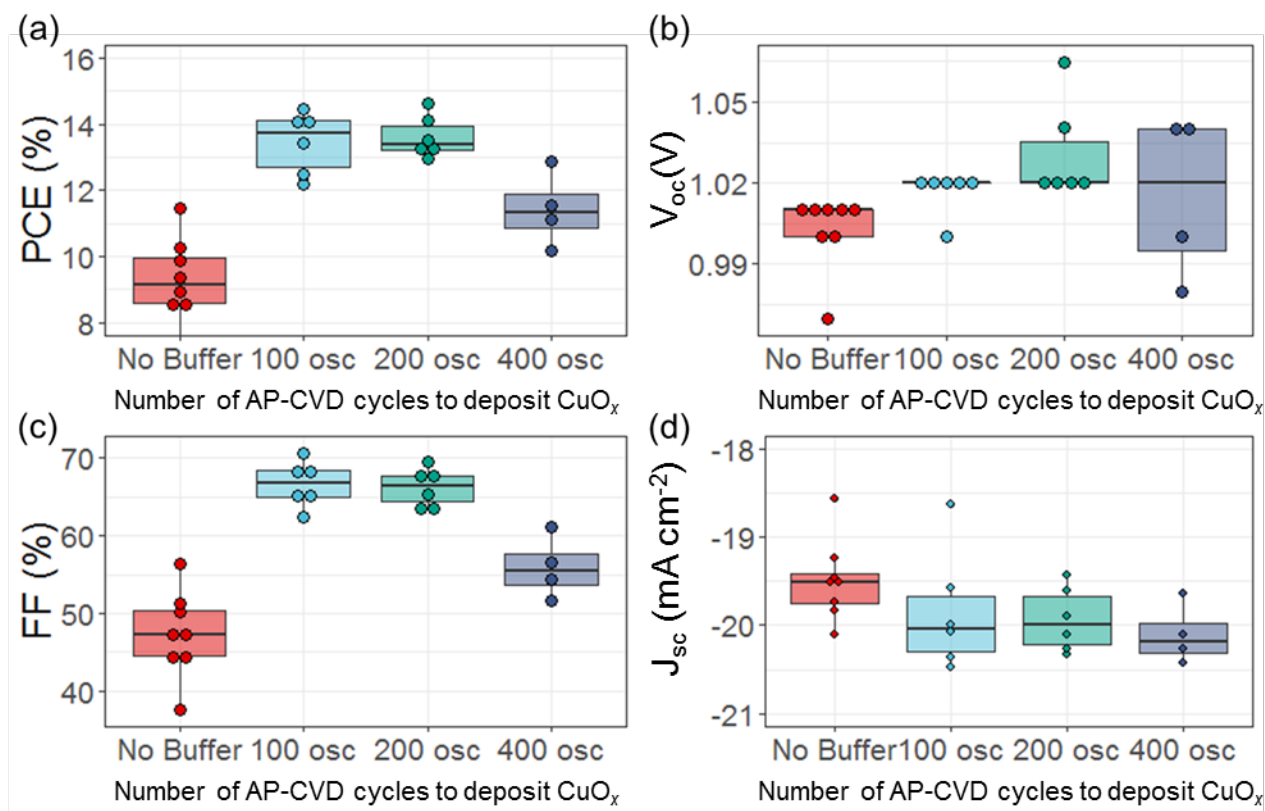
Figure S11. Boxplots summarizing the photovoltaic properties of semi-transparent devices without (red; 8 devices) and with CuO_x buffer layer (blue; 6 devices, green; 6 devices, dark blue; 5 devices). The photovoltaic properties are (a) power conversion efficiency, (b) open circuit voltage (V_{OC}), (c) fill factor (FF) and (d) short circuit current density (J_{SC}). Based on the growth rate, 100, 200 and 400 oscillations correspond to 3, 5 and 8 nm thick films. For these devices, the mp-TiO_x was not treated with Li-TFSI, leading to slightly lower device efficiencies than in Figure S10.

Table S2. Comparison of the champion performance of semi-transparent devices based on lead-halide perovskites with state-of-the-art efficiencies. The device structure, absorber layer material, efficiency and the average transmittance (and the wavelength averaged over) are shown.

| Structure	Bottom electrode/ ETL or HTL	Absorber layer	ETL or HTL / buffer layer/ top electrode	PCE (%)	T (%), spectral region [nm]	Ref.
p-i-n	ITO / PTAA	$Cs_{0.05}FA_{0.8}MA_{0.15}$ $PbI_{2.55}Br_{0.4}$	C_{60}/SnO$_2$/ZTO/IZO	18.2	75% , 760-1200	3
p-i-n	In$_2$O$_3$:H / PTAA	$MAPbI_3$	PCBM / ZnO/ ZnO:Al / Ni /Al	16.1	80%, 800 - 1200	4
p-i-n	ITO / PTAA	$MAPbI_3$	PCBM / C$_{60}$ / BCP / Cu / Au / BCP	16.5	62%, 800 - 1000	5
p-i-n	ITO /polyTPD/PFN	triple-cation perovskite	LiF/C$_{60}$/SnO/ZTO/ ITO	18.5	80% 800-1000	6
n-i-p	FTO / c-TiO$_2$ / mp-TiO$_2$	Rb-FA$_{0.75}$MA$_{0.15}$ Cs$_{0.1}$ PbI$_2$Br	PTAA / MoO$_x$ / ITO	16	84%, 720-1100	7
n-i-p	FTO / SnO$_2$	$Cs_{0.05}(MA_{0.17}FA_{0.83})_{0.95}$ $Pb(Br_{0.17}I_{0.83})_3$	Spiro-OMeTAD / Ag / ITO	17.7	70%, 800-1000	8
n-i-p	FTO / c-TiO$_2$ / mp-TiO$_2$	$Cs_{0.05}Rb_{0.05}Fa_{0.77}MA_{0.14}$ $PbI_{2.55}Br_{0.44}$	Spiro-OMeTAD / MoO$_x$ / IZO / Au	18.1	80%, 800-1200	9
n-i-p	FTO / c-TiO$_2$ / mp-TiO$_2$	2D/3D perovskite	Spiro-OMeTAD / MoO$_x$ / IZO	17.0	80% 800-1000	10
n-i-p	FTO / c-TiO$_2$ / mp-TiO$_2$	$Cs_{0.05}(MA_{0.17}FA_{0.83})_{0.95}$ $Pb(Br_{0.17}I_{0.83})_3$	PTAA / Cu$_2$O / ITO	16.7	73%, 800-1000	This work
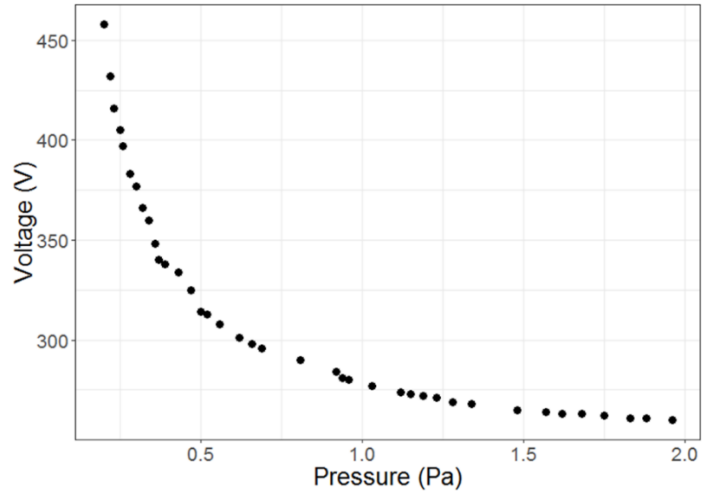
Figure S12. Voltage across target and chamber during sputtering at different pressures.
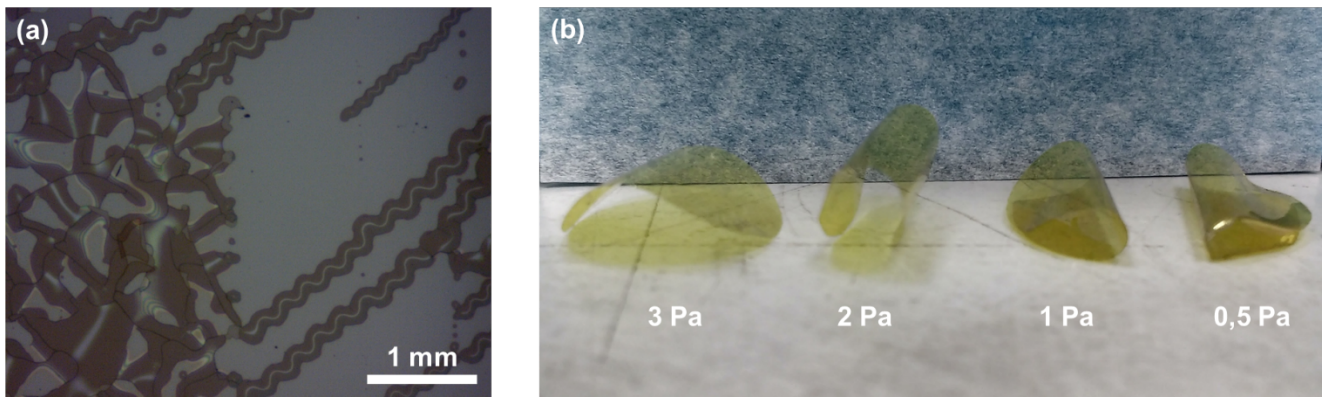

Figure S13. (a) Optical microscopy image of ITO deposited onto glass at 0.4 Pa. (b) Photograph

of 7 μm thick polyimide films with ITO deposited at 3 Pa, 2 Pa, 1 Pa and 0.5 Pa.

S3. Method for calculating the efficiency of four-terminal tandems

The four terminal efficiencies can also be calculated based on the efficiency and transmittance of the top cell, the EQE of the bottom cell and the efficiency of the bottom cell.

The short circuit current of a solar cell, after the light has been filtered through a filter with transmittance T, is given by

$$J_{sc} = -q \int_0^\infty T(\lambda) \, \text{EQE}(\lambda) \, \phi_{\text{ph}, \lambda}^{\text{AM1.5}} \, d\lambda, \tag{S1}$$

where q is the elemental charge, the EQE is the external quantum efficiency of the solar cell, $\phi_{\text{ph}, \lambda}^{\text{AM1.5}}$ is the AM1.5 spectral photon flux and λ is the wavelength.

The total calculated tandem power conversion efficiency is now given by

$$\text{PCE} = P_{\text{top cell}} + P_{\text{bottom cell}} = P_{\text{top cell}} + \frac{J_{sc} \, V_{oc} FF}{P_{\text{in}}}. \tag{S2}$$

S4. Derivation of the thermalization distance

Let the thermalization distance be defined as the average distance an atom originating from the target needs to travel in its original direction in order to reduce its initial velocity to the average velocity of the background gas. To derive this let us first consider the average mean free path of an atomic species S, with mass M_s, in thermal equilibrium with the background gas with atomic mass M_g. The average mean free path λ of the S is given by Eq. S3:[11]

$$\lambda^{-1} = \sqrt{2}\pi N_s \sigma_s^2 + \frac{1}{4}\pi N_g (\sigma_s + \sigma_g)^2 (1 + M_s/M_g)^{1/2}, \tag{S3}$$

where N_s and N_g are the gas densities of the sputtered and background gas, and σ_s and σ_g are the kinetic atomic diameters. In the case of sputtering the number of atomic species S is very small compared to the number of background gas atoms. There we can set $N_s << N_g$ and we can rewrite the equation of the mean free path into:

$$\lambda^{-1} = 8.34 \times 10^{14} \rho \, \frac{(\sigma_s + \sigma_g)^2}{4}(1 + M_s/M_g)^{1/2}. \tag{S4}$$

The fraction of the initial velocity that the atomic species S retain after colliding and maintaining its initial direction is called the velocity persistence v. It can be written as[12]

$$\nu = \frac{1-\mu}{1+\mu} + \frac{2\mu}{1+\mu} \cdot \nu_e, \tag{S5}$$

where $\mu = M_g/M_s$ and ν_e can be written as

$$\nu_e = \frac{\ln\left(\sqrt{1+\mu^2} + \mu\right)}{4\mu^3\sqrt{1+\mu^2}} + \frac{2\mu^8 + 5\mu^6 + 3\mu^4 - \mu^2 - 1}{4\mu^2(1+\mu^2)^3}. \tag{S6}$$

The number of collisions required to reduce the initial velocity of the atomic species S, here defined as v_o, to the average thermal velocity of the background gas, here defined as v_g, can be written as[13]

$$n = \frac{\ln(v_g/v_o)}{\ln(\nu)}. \tag{S7}$$

Note that this is the number of collisions required for atoms S which are traveling in their original direction. The thermal velocities are obtained from their initial energy and the average thermal energy at room temperature from

$$v = \sqrt{2E/m}.$$ (S8)

The mean free path of the atomic species S traveling through the background gas initially is not in thermal equilibrium with the background gas. The capture cross section and hence the mean free path is energy dependent. Therefore the mean free path of the atomic species originating from the target, λ_s, satisfies the following relation[12]

$$\lambda \leq \lambda_s \leq \sqrt{2}\lambda.$$ (S9)

So initially the mean free path can be up to 40% larger compared to the case when the sputtered atomic species are in thermal equilibrium with the background gas. To account for this we will assume an average value for λ_s of $1.25\ \lambda$.[12]

The thermalization distance can now be written as

$$D \approx 1.25\ n\ \lambda.$$ (S10)

Taking for the kinetic atomic diameters the following[11]

$\sigma_{Ar} = 0.29\ nm,$

$\sigma_O = 0.25\ nm,$

$\sigma_{In} = 0.37\ nm,$

$\sigma_{Sn} = 0.38\ nm,$

we obtain the mean free path for the different atomic species as a function of the background Argon pressure as shown in Figure S14. The persistence velocity as a function of the atomic mass taking argon as the background gas is depicted in Figure S15. Finally in Figure S16, we plot the number of required collision to thermalize atomic species as a function of the ratio of their atomic mass with respect to the atomic mass of the background gas.
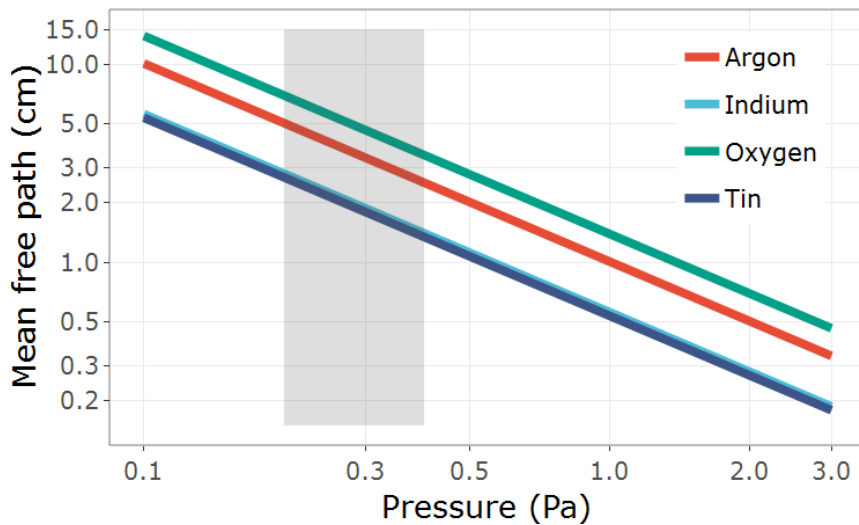

Figure S14. Mean free path of atomic argon (red), indium (blue), oxygen (green) and tin (dark blue) as a function of the argon gas background pressure. The grey shaded area indicates the region typically used in sputtering of transparent conductive oxides used in semi-transparent perovskite solar cells.
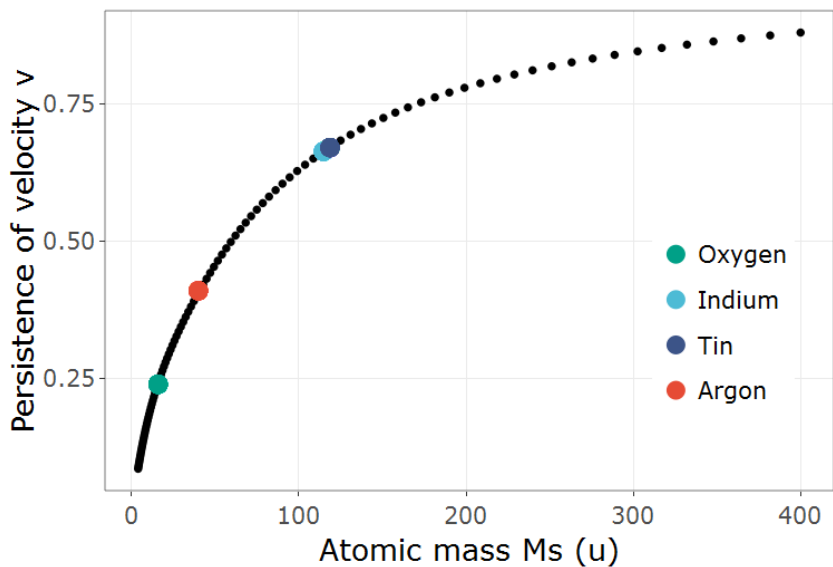
Figure S15. The calculated persistence velocity as a function of the atomic mass taking argon as the background gas. The atomic numbers for oxygen (green), indium (blue), tin (dark blue) and argon (red) are highlighted.
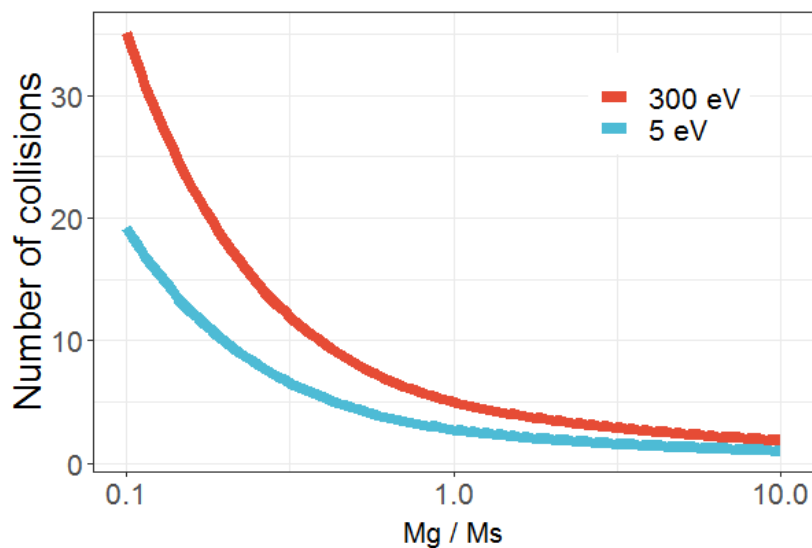

Figure S16. The calculated number of required collisions to thermalize the atomic species coming from the target as a function of M_g/M_s for an initial kinetic energy of 5 eV (blue) and 300 eV (red).

References

(1)   Hoye, R. L. Z.; Muñoz-Rojas, D.; Musselman, K. P.; Vaynzof, Y.; MacManus-Driscoll, J. L. Synthesis and Modeling of Uniform Complex Metal Oxides by Close-Proximity Atmospheric Pressure Chemical Vapor Deposition. *ACS Appl. Mater. Interfaces* **2015**, *7* (20), 10684–10694. https://doi.org/10.1021/am5073589.

(2)   Giordano, F.; Abate, A.; Correa Baena, J. P.; Saliba, M.; Matsui, T.; Im, S. H.; Zakeeruddin, S. M.; Nazeeruddin, M. K.; Hagfeldt, A.; Graetzel, M. Enhanced Electronic Properties in Mesoporous TiO2 via Lithium Doping for High-Efficiency Perovskite Solar Cells. *Nat. Commun.* **2016**, *7*, 10379. https://doi.org/10.1038/ncomms10379.

(3)   Tong, J.; Song, Z.; Kim, D. H.; Chen, X.; Chen, C.; Palmstrom, A. F.; Ndione, P. F.; Reese, M. O.; Dunfield, S. P.; Reid, O. G.; Liu, J.; Zhang, F.; Harvey, S. P.; Li, Z.; Christensen, S. T.; Teeter, G.; Zhao, D.; Al-Jassim, M. M.; Van Hest, M. F. A. M.; Beard, M. C.; Shaheen, S. E.; Berry, J. J.; Yan, Y.; Zhu, K. Carrier Lifetimes of >1 ms in Sn-Pb Perovskites Enable Efficient All-Perovskite Tandem Solar Cells. *Science* **2019**, *364* (6439), 475–479. https://doi.org/10.1126/science.aav7911.

(4)   Fu, F.; Feurer, T.; Weiss, T. P.; Pisoni, S.; Avancini, E.; Andres, C.; Buecheler, S.; Tiwari, A. N. High-Efficiency Inverted Semi-Transparent Planar Perovskite Solar Cells in Substrate Configuration. *Nat. Energy* **2017**, *2*, 16190. https://doi.org/10.1038/nenergy.2016.190.

(5)   Chen, B.; Bai, Y.; Yu, Z.; Li, T.; Zheng, X.; Dong, Q.; Shen, L.; Boccard, M.; Gruverman, A.; Holman, Z.; Huang, J. Efficient Semitransparent Perovskite Solar Cells for 23.0%-Efficiency Perovskite/Silicon Four-Terminal Tandem Cells. *Adv. Energy Mater.* **2016**, *6* 1601128. https://doi.org/10.1002/aenm.201601128.

(6)   Xu, J.; Boyd, C. C.; Yu, Z. J.; Palmstrom, A. F.; Witter, D. J.; Larson, B. W.; France, R. M.; Werner, J.; Harvey, S. P.; Wolf, E. J.; Weigand, W.; Manzoor, S.; Hest, M. F. A. M. Van; Berry, J. J.; Luther, J. M.; Holman, Z. C.; Mcgehee, M. D. Triple-Halide Wide–Band Gap Perovskites with Suppressed Phase Segregation for Efficient Tandems. *Science* **2020**, *367* (1104), 1097–1104.

(7)   Duong, T.; Wu, Y. L.; Shen, H.; Peng, J.; Fu, X.; Jacobs, D.; Wang, E. C.; Kho, T. C.; Fong, K. C.; Stocks, M.; Franklin, E.; Blakers, A.; Zin, N.; McIntosh, K.; Li, W.; Cheng, Y. B.; White, T. P.; Weber, K.; Catchpole, K. Rubidium Multication Perovskite with Optimized Bandgap for Perovskite-Silicon Tandem with over 26% Efficiency. *Adv. Energy Mater.* **2017**, *8*, 1700228. https://doi.org/10.1002/aenm.201700228.

(8)   Dewi, H. A.; Wang, H.; Li, J.; Thway, M.; Sridharan, R.; Stangl, R.; Lin, F.; Aberle, A. G.; Mathews, N.; Bruno, A.; Mhaisalkar, S. Highly Efficient Semitransparent Perovskite Solar Cells for Four Terminal Perovskite-Silicon Tandems. *ACS Appl. Mater. Interfaces* **2019**, *11* (37), 34178–34187. https://doi.org/10.1021/acsami.9b13145.

(9)   Shen, H.; Duong, T.; Peng, J.; Jacobs, D.; Wu, N.; Gong, J.; Wu, Y.; Karuturi, S. K.; Fu, X.; Weber, K.; Xiao, X.; White, T. P.; Catchpole, K. Mechanically-Stacked Perovskite/CIGS Tandem Solar Cells with Efficiency of 23.9% and Reduced Oxygen Sensitivity. *Energy Environ. Sci.* **2018**, *11* (2), 394–406. https://doi.org/10.1039/c7ee02627g.

(10)   Duong, T.; Pham, H.; Kho, T. C.; Phang, P.; Fong, K. C.; Yan, D.; Yin, Y.; Peng, J.; Mahmud, A.; Gharibzadeh, S.; Nejand, B. A.; Hossain, I. M.; Khan, M. R.; Mozaffari, N.; Wu, Y.; Shen, H.; Zheng, J.; Mai, H.; Liang, W.; Samundsett, C.; Stocks, M.; Mcintosh, K.;

Andersson, G. G.; Lemmer, U.; Richards, B. S.; Paetzold, U. W.; Ho-ballie, A.; Liu, Y.; Macdonald, D.; Blakers, A.; Wong-leung, J.; White, T.; Weber, K.; Catchpole, K. High Efficiency Perovskite-Silicon Tandem Solar Cells : Effect of Surface Coating versus Bulk Incorporation of 2D Perovskite. *Adv. Energy Mater.* **2020**, *10*, 1903553. https://doi.org/10.1002/aenm.201903553.

(11)   McDaniel, E. W. *Collision Phenomena in Ionized Gases*; 1964.

(12)   Jeans, J. H. *An Introduction To The Kinetic Theory of Gases, Ch10*; 1940.

(13)   Westwood, W. D. Calculation of Deposition Rates in Diode Sputtering Systems. *J Vac Sci Technol* **1978**, *15* (1), 569429. https://doi.org/10.1116/1.569429.